Science
AAAS

Supplementary Materials for

Metastable Dion-Jacobson 2D structure enables efficient and stable perovskite solar cells

Fei Zhang *et al.*

Corresponding authors: Fei Zhang, fei.zhang@nrel.gov; Yanfa Yan, yanfa.yan@utoledo.edu; Bryon W. Larson, bryon.larson@nrel.gov; Kai Zhu, kai.zhu@nrel.gov

DOI: 10.1126/science.abj2637

The PDF file includes:

Materials and Methods
Figs S1 to S30
Tables S1 to S7
References

Materials and Methods

Materials

Lead oxide (PbO, 99.999%), 1,3-propanediamine, N,N-dimethyl-1,3-propane diamine, N,N-anhydrous dimethylformamide (DMF), ethanol, 2-propanol (IPA), chlorobenzene (CB), dimethyl sulfoxide (DMSO) and 57% aqueous hydriodic acid (HI) solution (99.95%, distilled, stabilized by H_3PO_2) were purchased from Sigma-Aldrich and used as-received without any other refinement unless otherwise specified. Formamidinium iodide (FAI), methylammonium bromide (MABr), methylammonium chloride (MACl), and 1,4-butane diammonium iodide ($BDAI_2$) were purchased from Greatcell Solar. Lead iodide (PbI_2) and lead bromide ($PbBr_2$) were from TCI Corporation. 2,2',7,7'-Tetrakis[N,N-di(4-methoxyphenyl)amino]-9,9'-spirobifluorene (spiro-OMeTAD) was received from Merck Corporation. The titanium diisopropoxide bis(acetylacetonate), bis(trifluoromethanesulfonyl)imide lithium salt, poly(triarylamine) (PTAA), tert-butylpyridine, and cesium iodide (CsI) were purchased from Sigma-Aldrich. 4-isopropyl-4'-methyldiphenyliodoniumtetrakis (pentafluorophenyl)borate (TPFB) was purchased from Lumtec. Substrates are patterned fluorine-doped tin-oxide-coated glass (<15 Ω /square) obtained from Advanced Election Technology Co., Ltd.

Synthesis of 1,3-propane diammonium diiodine ($PDAI_2$) and N,N-dimethyl-1,3-propane diammonium diiodide ($DMePDAI_2$)

5 mL of 1,3-propanediamine or N,N-dimethyl-1,3-propane diamine was first mixed with 15 mL ethanol (200 Proof), and the solution was placed in an ice water bath (0 °C). 20 mL HI solution was slowly added to the PDA solution (dropwise). The mixture was allowed to stir for 2 hours. After the reaction, solvents were removed by vacuum and white powders were collected by vacuum filtration. The product was recrystallized from ethanol/diethyl ether and dried in vacuum overnight. $DMePDAI_2$ was synthesized following the same process.

Synthesis of $[PDAPbI_4]_{15}\bullet[PDAI_2]$ single crystals

335 mg (1.5 mmol) of PbO and 492 mg (1.5 mmol) of $PDAI_2$ were fully dissolved in 6 mL of HI solution at 90 °C. The solution was then slowly cooled to room temperature at a rate of 1 °C/h, giving yellow crystals. The crystals were then isolated from the parent solution by vacuum filtration and dried under vacuum.

Synthesis of $BDAPbI_4$ single crystals

335 mg (1.5 mmol) of PbO and 516 mg (1.5 mmol) of $BDAI_2$ were fully dissolved in 6 mL of HI solution at 90 °C. The solution was then slowly cooled to room temperature at a rate of

1 °C/h, giving yellow crystals. The crystals were then isolated from the parent solution by vacuum filtration and dried under vacuum.

Synthesis of $DMePDAPbI_4$-1 single crystals

335 mg (1.5 mmol) of PbO and 537 mg (1.5 mmol) of $DMePDAI_2$ were fully dissolved in 6 mL of HI solution at 90 °C. The solution was then slowly cooled to room temperature at a rate of 1 °C/h, giving red crystals. The crystals were then isolated from the parent solution by vacuum filtration and dried under vacuum.

Synthesis of $DMePDAPbI_4$-2 single crystals

335 mg (1.5 mmol) of PbO and 537 mg (1.5 mmol) of $DMePDAI_2$ are fully dissolved in 6 mL of HI solution at 90 °C. The solution is then cooled to room temperature without controlling the rate, giving red crystals. The crystals are then isolated from the parent solution by vacuum filtration and dried under vacuum.

2D (n=1) perovskites-based device fabrication

Devices were prepared on conductive fluorine-doped tin oxide (FTO)-coated glass substrates. The substrates were cleaned extensively by deionized water, acetone, and isopropanol. A compact titanium dioxide (TiO_2) layer about 40 nm thick was deposited by spray pyrolysis of 7 mL of 2-propanol solution containing 0.6 mL of titanium diisopropoxide bis(acetylacetonate) solution (75% in 2-propanol, Sigma-Aldrich) and 0.4 mL of acetylacetone at 450 °C in air. The precursor solutions were prepared by mixing PbI_2 and $BDAI_2$ or $DMePDAI_2$, and PEAI or BAI at a stoichiometric ratio of 1:1 and 1:2, respectively, with a concentration of 0.35 mol/L in DMF. The spin-coating procedure was performed at 4,000 rpm for 30 s. Thereafter, the substrate was put onto a hotplate for 15 min at 100 °C. Subsequently, the hole-transporting layer (HTM) was deposited on the top of the perovskite by spin coating at 4,000 rpm for 15 s. The spiro-OMeTAD solutions were prepared by dissolving the spiro-OMeTAD in 1-mL CB at a concentration of 77.6 mg/mL, with the addition of 20.6 μL bis(trifluoromethanesulfonyl)imide lithium salt from a stock solution in acetonitrile, 35.5 μL of tert-butylpyridine. The fabrication of perovskite layer and HTM layer of devices were executed in a dry air box, where the variation of humidity is from about 1% to 4%, the variation of temperature is from about 20 °C to 24 °C. The devices were finalized by thermal evaporation of 100-nm gold.

$FA_{0.85}MA_{0.1}Cs_{0.05}PbI_{2.9}Br_{0.1}$-based device fabrication

Devices were prepared on conductive FTO-coated glass substrates. The substrates were cleaned extensively by deionized water, acetone, and isopropanol. A compact titanium dioxide (TiO_2) layer of about 40 nm was deposited by spray pyrolysis of 9-mL ethanol solution containing

0.6-mL titanium diisopropoxide bis(acetylacetonate) solution (75% in 2-propanol, Sigma-Aldrich) and 0.4-mL acetylacetone at 450 °C in air. On top of this layer, mesoporous titanium dioxide was formed by spin-coating 30-nm-sized nanoparticles (Dyesol 30NRD, Dyesol) diluted in ethanol (1:5.5 *w*/*w*) at 4,500 rpm for 15 s. The $FA_{0.85}MA_{0.1}Cs_{0.05}PbI_{2.9}Br_{0.1}$ precursor solution was prepared in a glovebox from a 1.60 M $Pb^{2+}$with 5% excess of PbI_2 and in the mixed solvent of DMF and DMSO; the volume ratio of DMF/DMSO was 4:1. The spin-coating procedure was performed at 2,000 rpm for 10 s followed by 6,000 rpm for 30 s. At 15 s before the last spin-coating step, 140 μL of chlorobenzene were pipetted onto the substrate. Thereafter, the substrate was put onto a hotplate for 20 minutes at 120 °C; these are identified as the "control" samples. For $DMePDAI_2$ treatment, different concentrations of $DMePDAI_2$ were dissolved in IPA and spin-coated on the surface of the perovskite at 3000 rpm for 30 s with subsequent annealing for 2 mins at 100 °C. The best condition is designated "$DMePDAI_2$" samples. Subsequently, the HTM was deposited on top of the perovskite by spin coating at 4,500 rpm for 15 s. The spiro-OMeTAD solutions were prepared by dissolving the spiro-OMeTAD in 1-mL CB at a concentration of 77.6 mg/mL, with the addition of 20.6 μL bis(trifluoromethanesulfonyl)imide lithium salt from a stock solution in acetonitrile, 35.5 μL of tert-butylpyridine. For the high humidity/heat stability test, PTAA solution was prepared from 16 mg of PTAA and 1.8 mg of TPFB in 0.8 mL of CB and kept under stirring over 1h before using it. The PTAA was deposited on top of perovskite by spin-coating at 1500 rpm for 30 sec. The devices were finalized by thermal evaporation of 100-nm gold.

$FA_{0.97}MA_{0.03}PbI_{2.91}Br_{0.09}$-based device fabrication

FTO glass substrates were washed by ultrasonication in water with detergent, clean water, and 2-propanol sequentially. The SnO_2 electron transport layer was deposited using the chemical bath deposition method (*34*), and the resulting sample was annealed at 150 °C for 2 h. The perovskite precursor solution was prepared by mixing 1.55 M PbI_2, 1.55 M FAI 0.048 M $MAPbBr_3$ and 0.5 M MACl in a mixed solvent (DMF/DMSO = 8:1). Then the perovskite precursor solution was deposited onto the UV-ozone treated SnO_2 film at 5000 rpm for 20s, where 1 mL of diethyl ether was dropped on the rotating film 10 s after spinning. The resulting film was annealed at 150 °C for 15 min and 100 °C for 5 min, sequentially. For $DMePDAI_2$ treatment, 200 μL of 0.5 mg/mL $DMePDAI_2$ in IPA was spin-coated on perovskite film at 3000 rpm for 30 s with subsequent annealing for 2 mins at 100 °C. The spiro-OMeTAD layer was deposited on the perovskite layer by spin coating the spiro-OMeTAD stock solution at 4000 rpm for 30 s. Finally, a 100 nm Au electrode layer was deposited by thermal evaporation.

$MAPbI_3$-based device fabrication

Devices were prepared on conductive FTO-coated glass substrates. The substrates were cleaned extensively by deionized water, acetone, and isopropanol. A compact titanium dioxide

(TiO_2) layer of about 40 nm was deposited by spray pyrolysis of 9-mL ethanol solution containing 0.6-mL titanium diisopropoxide bis(acetylacetonate) solution (75% in 2-propanol, Sigma-Aldrich) and 0.4-mL acetylacetone at 450 °C in air. On top of this layer, mesoporous titanium dioxide was formed by spin-coating 30-nm-sized nanoparticles (Dyesol 30NRD, Dyesol) diluted in ethanol (1:5.5 *w*/*w*) at 4,500 rpm for 15 s. The $MAPbI_3$ precursor solution was prepared in a glovebox from a 1.45 M $Pb^{2+}$with 5% excess of PbI_2 and in the mixed solvent of DMF and DMSO; the volume ratio of DMF/DMSO was 4:1. The spin-coating procedure was performed at 2,000 rpm for 10 s followed with 6,000 rpm for 30 s. At 15 s before the last spin-coating step, 140 μL of CB were pipetted onto the substrate. Thereafter, the substrate was put onto a hotplate for 30 minutes at 100 °C. For $DMePDAI_2$ treatment, the 200 μL of 0.5 mg/ml $DMePDAI_2$ in IPA was spin-coated onto the perovskite film at 3000 rpm for 30 s with subsequent annealing for 2 mins at 100 °C. Subsequently, the HTM was deposited on top of the perovskite by spin coating at 4,500 rpm for 15 s. The devices were finalized by thermal evaporation of 100-nm gold.

Perovskite film and device characterizations

SEM (FEI Nova 630, field-emission gun) imaging was performed with an electron-beam voltage of 3 kV in the immersion-lens mode. The X-ray diffraction (XRD) and grazing incident XRD (GIXRD) of the perovskite films was characterized using a Rigaku D-Max 2200 diffractometer with Cu Kα radiation. The optical absorption spectra of perovskite films were measured using an ultraviolet/visible (UV/Vis) spectrophotometer (Cary6000i). Water contact angles of perovskite films were measured using a JC 2000D contact angle instrument. Solar cell performance measurements were taken under a simulated AM 1.5G illumination (100 mW/cm^2, Oriel Sol3A Class AAA Solar Simulator). The photocurrent density-voltage (J-V) characteristics were measured using a Keithley 2400 source meter. The J-V curves of all devices were measured by masking the active area with a metal mask of area 0.12 cm^2. Both backward-scan and forward-scan curves were measured with a bias step of 10 mV and delay time of 0.05 s. The continuous current and power output were measured using a potentiostat (Princeton Applied Research, Versa STAT MC). External quantum efficiency (EQE) spectra of solar cells were measured using a solar cell quantum-efficiency measurement system (QEX10, PV Measurements). Single-crystal structure analysis via XRD was performed on a Bruker D8 Venture Photon 2 diffractometer at the University of Kentucky and at the ALS on a Bruker D8 Photon 100 diffractometer. Stability measurements were performed with maximum power-point (MPP) tracking under continuous illumination from a full AM1.5 sun-equivalent white LED lamp in N_2 at about 40 °C. The TRMC measurements were performed according to our previous report (*28*).

Grazing incidence wide-angle X-ray scattering (GIWAXS) characterization

GIWAXS data were collected at beamline 11-3 at the Stanford Synchrotron Radiation Source (SSRL) at the SLAC National Accelerator Laboratory. The X-ray photon energy used at this beamline is 12.7 keV. Samples were exposed to the beam for 60 s in a sealed chamber under helium flow in grazing incidence geometry at an incident angle in the range of 0.12°–3.12°. A Rayonix MX225 CCD area detector was placed at a sample-to-detector distance of 200 mm. Collected data was calibrated against a reference sample (LaB_6) using a software package pyFAI (*35*). The same python package was used for the data processing to obtain 2D and integrated 1D diffraction patterns as a function of a scattering vector $q = \frac{4\pi}{\lambda}\sin\left(\frac{2\theta}{2}\right)$. The integration was performed between $0° < \chi < 90°$, where χ is the azimuthal angle.

Kelvin probe force microscopy (KPFM) and conductive atomic force microscopy (C-AFM) characterizations

The measurements were performed inside an Ar-filled glovebox with water and oxygen level lower than 0.01 ppm. All the scans were collected via Nanosensor PPP-EFM tips. The KPFM mappings have a spatial resolution of 30 nm and an electrical resolution of 10 mV. We directly cleaved the cells inside the glovebox with no exposure to air or polishing/ion-milling treatments to flatten the surface. Then, KPFM cross-section images were used for alignment to topography and to mark the locations of interfaces. C-AFM scans were all acquired using a single tip and the same scan conditions, at least two areas were examined to ensure the reliability of results. The FTO substrate was connected to the AFM stage and the applied bias voltage was 0.8 V.

X-ray and ultraviolet photoemission spectroscopy (XPS and UPS) characterizations

XPS measurements were performed on a Physical Electronics 5600 photoelectron spectrometer, which has been discussed in detail previously (*36*). Briefly, radiation was produced by a monochromatic 350 W Al Kα excitation centered at 1486.7 eV. XPS core-level spectra were collected using a step size of 0.1 eV and pass energy of 11.75 eV. The electron binding energy scale was calibrated using the Fermi edge of a copper substrate, cleaned with Argon ion bombardment. Peak areas were fit using a Gaussian-Lorentzian peak fitting algorithm with a Shirley background. Spectra taken with the Al source are typically assigned an uncertainty of 0.05 eV. Compositional analyses and deconvolutions are typically assigned an uncertainty of 5%. UPS measurements were performed on a Kratos Axis Ultra spectrometer using a He I excitation at 21.22 eV at a 5 eV pass energy and 0° take-off angle. Samples were biased at -10.00 V to accelerate low kinetic energy electrons and secondary electrons from the local environment. The Fermi level was calibrated using an Ar sputter-etched, atomically clean gold sample measured prior to characterization of the samples.

Computation

The electronic properties were calculated using screened hybrid functional and van der Waals (vdW) interaction (HSE+vdW) to account the effects of organic molecules (*26*). We also employed the Grimme-D3 method to account for the van der Waals (vdW) effect (*27*). The spin-orbit coupling is not included in all calculations due to the small effects on the valence band (*37, 38*). The calculations were performed with auxiliary density matrix method (ADMM) implemented in CP2K (*39, 40*).

Space-charge-limited-current (SCLC) characterization

Vertical hole-only devices (Au/perovskite/Au) were fabricated to extract the out-of-plane hole mobility of 2D perovskite single crystals (*41*, *42*). The dark J-V characteristics of hole-only devices were measured by a Keithley 2400 source. Mobilities were calculated at the SCLC region using Child’s law, $J = 9\varepsilon_0\varepsilon_T\mu_h V^2/8L^3$, where J is the current density, L is the active thickness of the 2D perovskite single crystals, μ_h is the hole mobility, ε_T is the relative dielectric constant of the transport medium, ε_0 is the permittivity of free space, V is the applied voltage to the device. Average values and standard deviations were obtained on 10 devices fabricated and tested under the same conditions.

Supplementary Figures

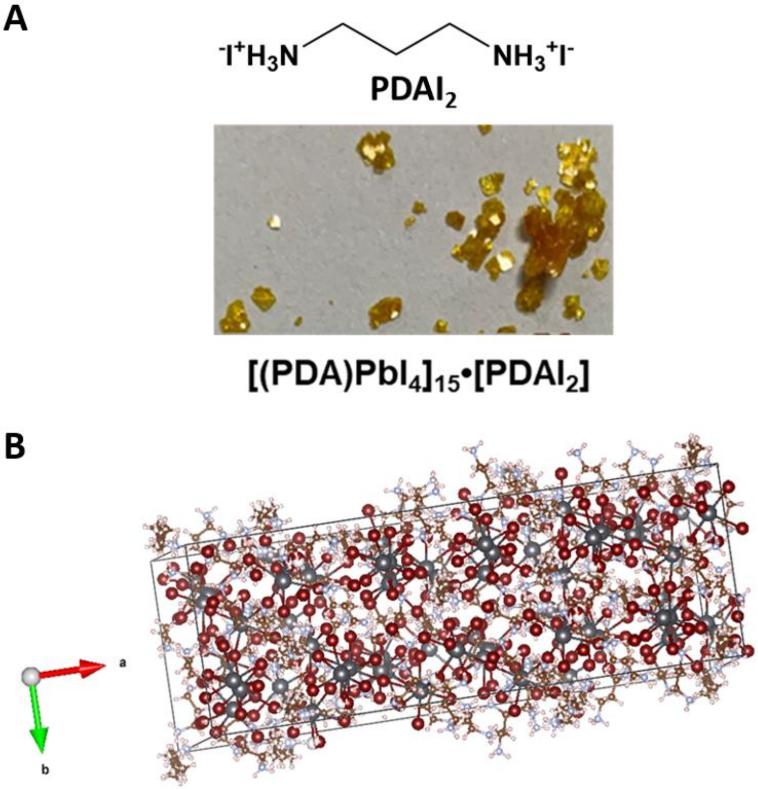

Fig. S1. (**A**) The chemical structure of 1,3-propane diammonium diiodine ($PDAI_2$) and the photo of single crystals of $[PDAPbI_4]_{15}•[PDAI_2]$. (**B**) The single-crystal structure of $[PDAPbI_4]_{15}•[PDAI_2]$. Note that when the halide is Br^-, the PDA^{2+} cannot form the typical 2D DJ phase perovskite; however, when the halide is Cl^-, the 2D $PDAPbCl_4$ can form, likely since Cl^- ions are much smaller and not as electrostatically repulsive at this distance as iodide or bromide (*43*).

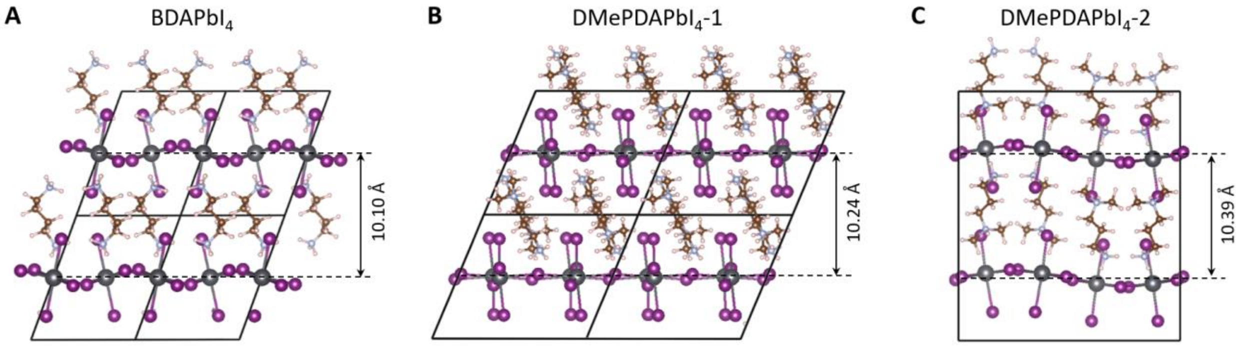

Fig. S2. Side view of the crystal structures of (A) BDAPbI$_4$, (B) DMePDAPbI$_4$-1, and (C) DMePDAPbI$_4$-2 single crystals. The average interlayer distances are indicated. The crystal structure of DMePDAPbI$_4$-2 was reported in reference (*22*).

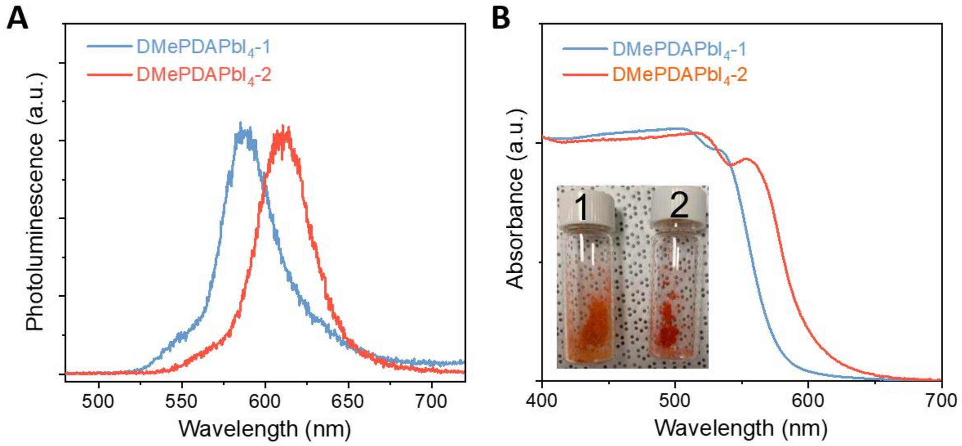

Fig. S3. (**A**) The photoluminescence (PL) spectra and (**B**) absorption spectra of DMePDAPbI$_4$-1 and DMePDAPbI$_4$-2 single crystal samples. The inset shows the photographs of DMePDAPbI$_4$-1 and DMePDAPbI$_4$-2 single crystal samples.

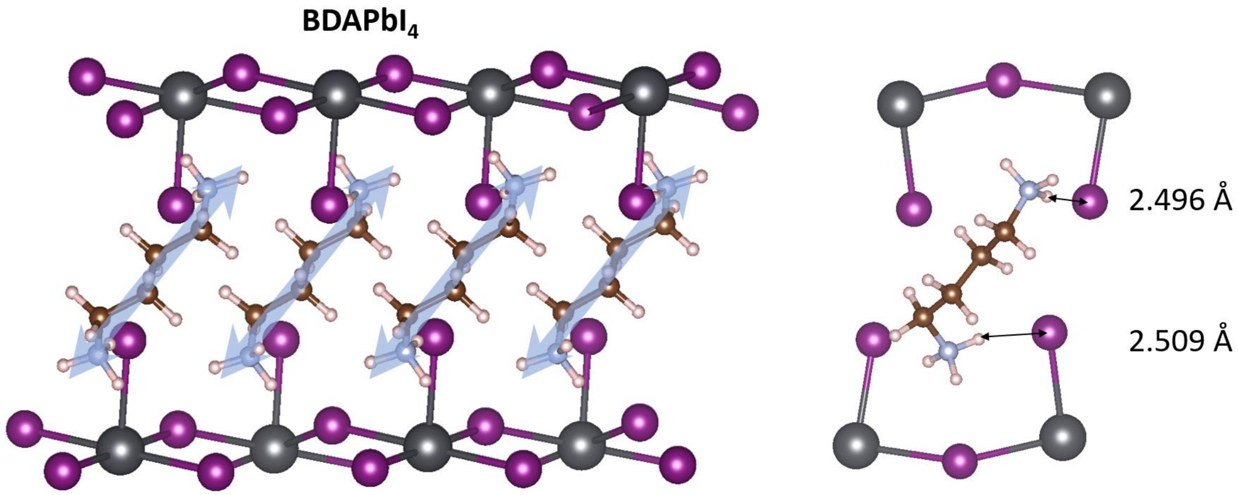

Fig. S4. Side view of the crystal structure of BDAPbI$_4$ and the corresponding hydrogen-bonding configuration.

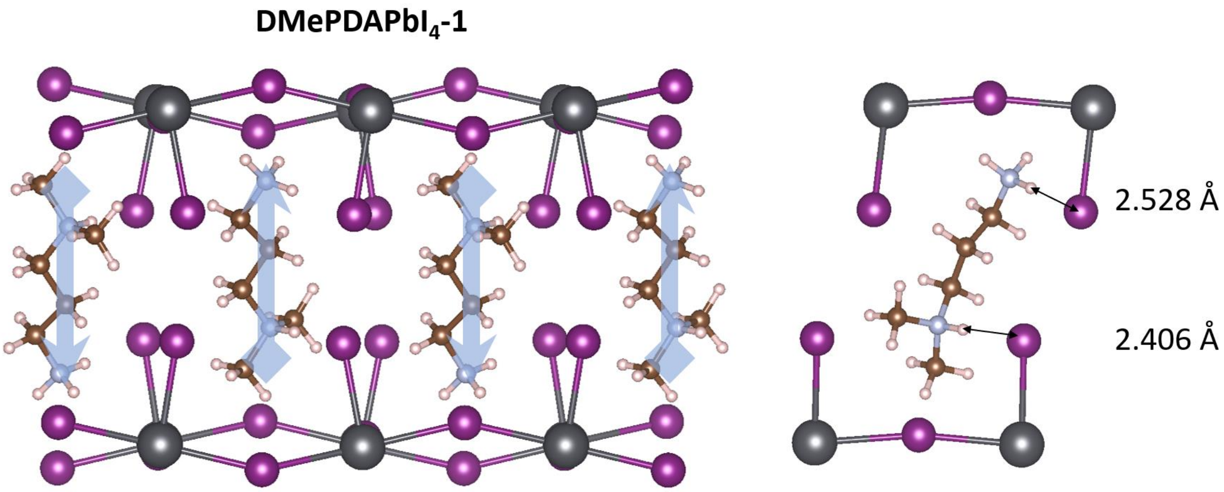

Fig. S5. Side view of the crystal structure of DMePDAPbI4-1 and the corresponding hydrogen-bonding configuration.

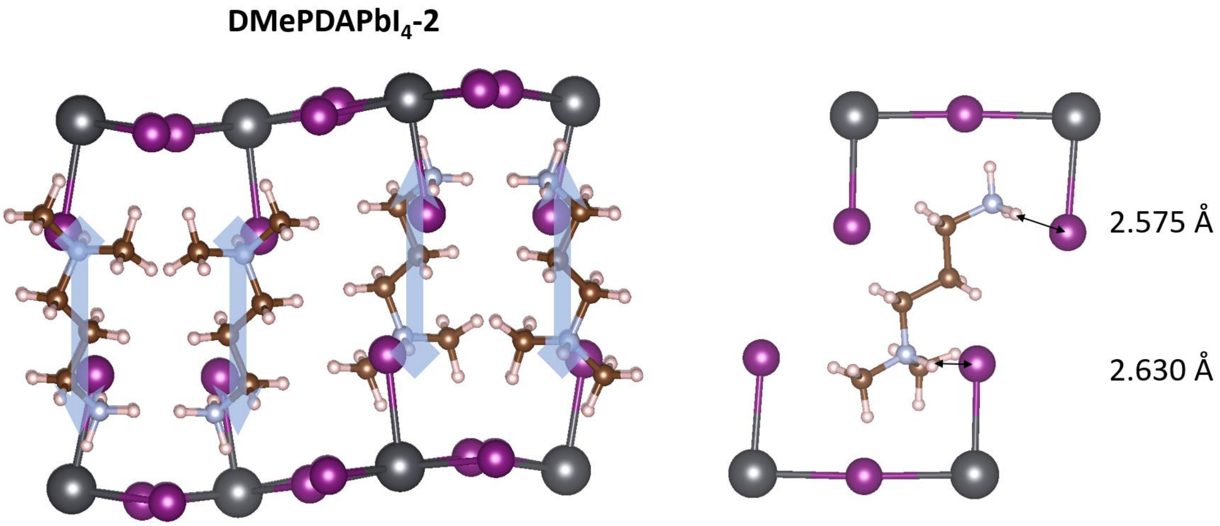

Fig. S6. Side view of the crystal structure of DMePDAPbI4-2 and the corresponding hydrogen-bonding configuration.

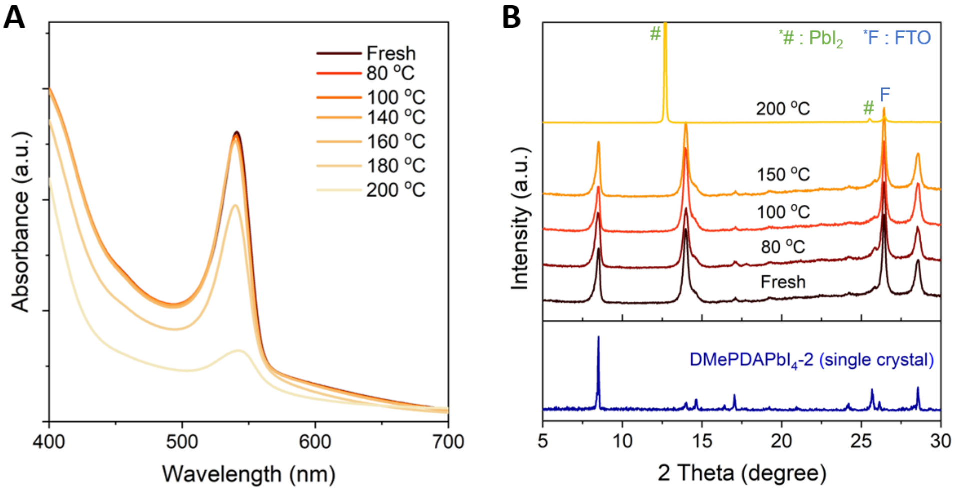

Fig. S7. Stability of DMePDAPbI$_4$-2 thin films subjected to elevated temperatures. (**A**) Absorption and (**B**) XRD patterns of the DMePDAPbI$_4$-2 thin films aged at different temperatures from 80°C to 200°C for 30 min. The sample annealed at 200°C showed a strong diffraction peak at 12.6° and 25.6°, corresponding to the (001) and (002) planes of the PbI$_2$ crystal. These results suggest that the metastable DMePDAPbI$_4$-2 structure is stable up to ~150°C, which is significantly higher than normal device operational temperatures. It is also clear from these results that DMePDAPbI$_4$-2 does not transition to DMePDAPbI$_4$-1 under these conditions, but rather decomposes to the lowest energy primary salts. The results are consistent with the calculated high transition energy barrier between the metastable and stable DMePDAPbI$_4$ structures.

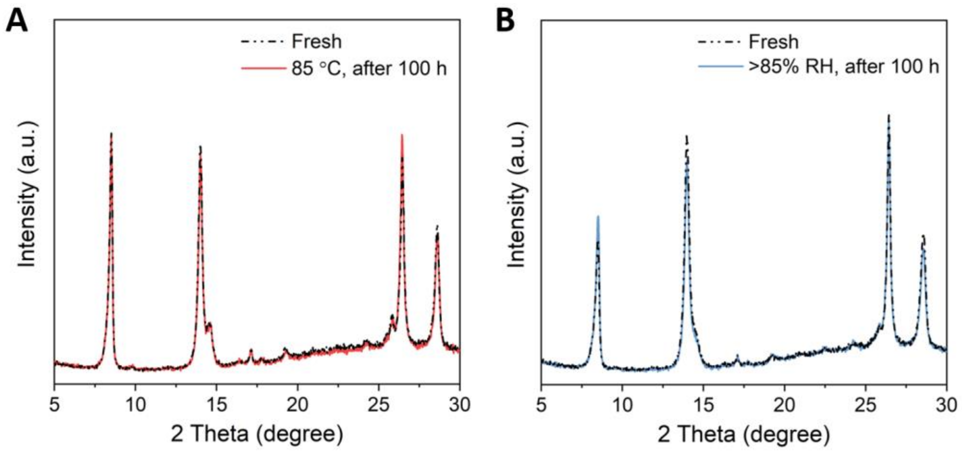

Fig. S8. XRD patterns before and after (**A**) thermal and (**B**) humidity ageing tests of the DMePDAPbI_4-2 thin films. For the thermal test, the samples were heated at 85°C for 100 h under ~5% relative humidity (RH) in dark. For the humidity test, the samples were aged for 100 h under >85% RH in dark.

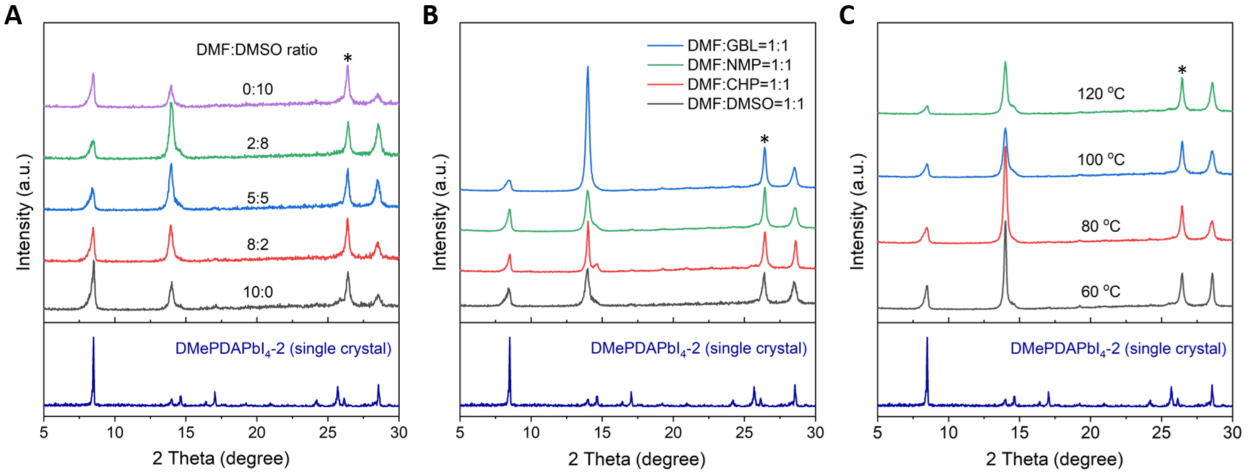

Fig. S9. Structure of solution grown DMePDAPbI4 thin films under various conditions. (**A**) Solvents with DMF:DMSO ratio changed from 0:10 to 10:0. (**B**) Solvents with different combinations of DMF:GBL, DMF:NMP, DMF:CHP (1-Cyclohexyl-2-pyrrolidone), and DMF:DMSO, all with 1:1 ratio. (**C**) Post-growth annealing temperature is varied from 60°C to 120°C. These results indicate that only the metastable DMePDAPbI4-2 film can be formed with the solution growth method.

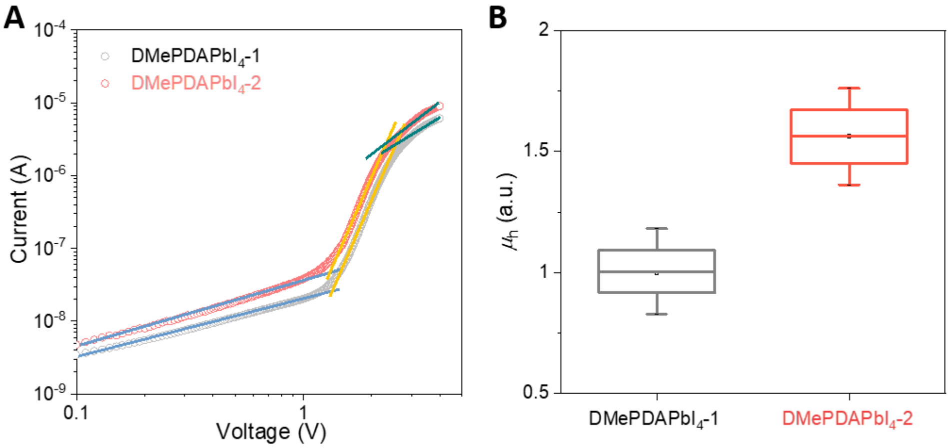

Fig. S10. Comparison of out-of-plane hole transport by SCLC. (**A**) Dark I-V characteristics of vertical hole-only devices based on 2D perovskite single crystals. (**B**) Statistical comparison of normalized out-of-plane hole mobilities.

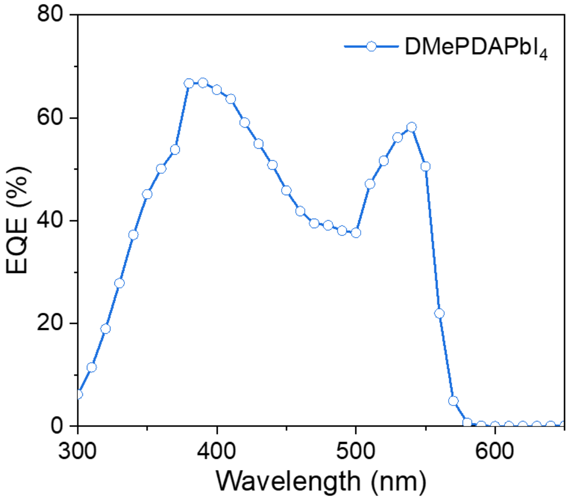

Fig. S11. External quantum efficiency (EQE) spectrum of $DMePDAPbI_4$ based perovskite solar cell using a stack of glass/FTO/TiO_2/$DMePDAPbI_4$/spiro-OMeTAD/Au.

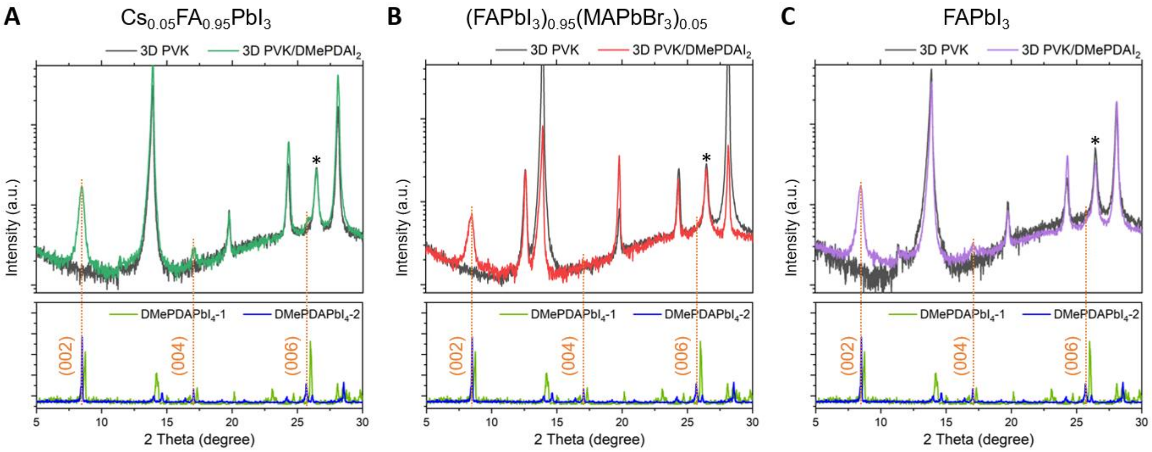

Fig. S12. GIXRD patterns of of perovskites without (3D PVK) and with DMePDAI$_2$ surface treatment (3D PVK/DMePDAI$_2$) using different perovskite compositions: (**A**) $Cs_{0.05}FA_{0.95}PbI_3$, (**B**) $(FAPbI_3)_{0.95}(MAPbBr_3)_{0.05}$, and (**C**) $FAPbI_3$. The peaks labeled with “*” are from the FTO substrate.

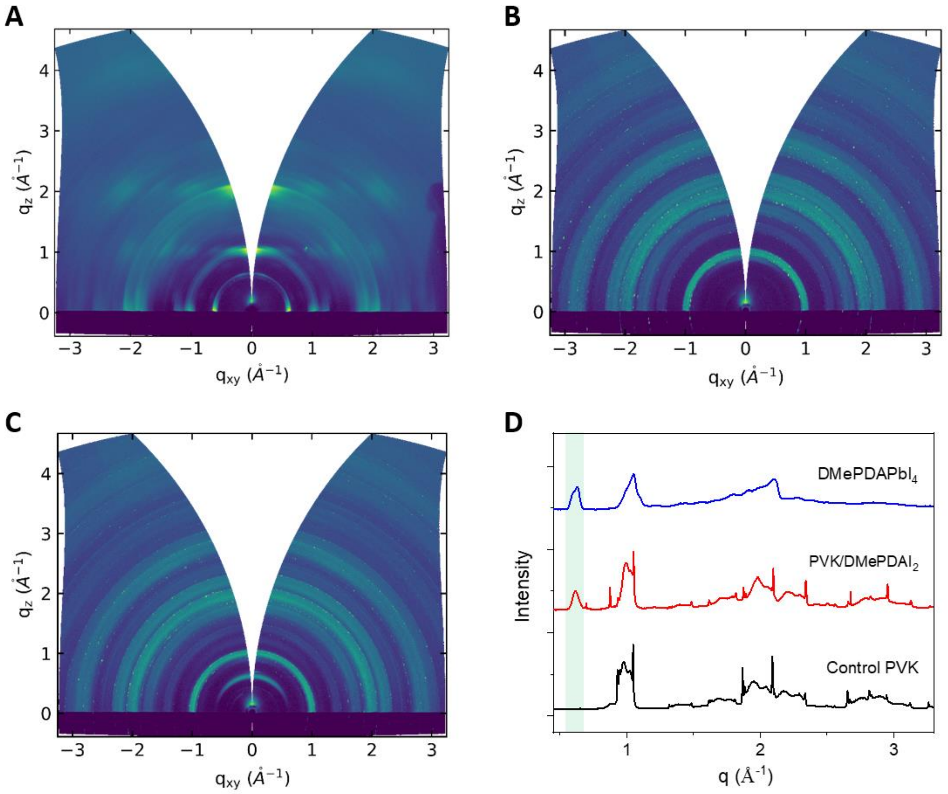

Fig. S13. GIWAXS of (**A**) DMePDAI$_4$, (**B**) control perovskite (Control PVK), and (**C**) DMePDAI$_2$ modified perovskite (PVK/DMePDAI$_2$) thin films. The incidence angle was 0.12°. (**D**) Radially integrated GIWAXS data from A-C. The low-angle diffraction peak at about q = 0.61 Å^{-1} corresponds to about 8.57° for the thin-film XRD measurement using Cu Kα radiation.

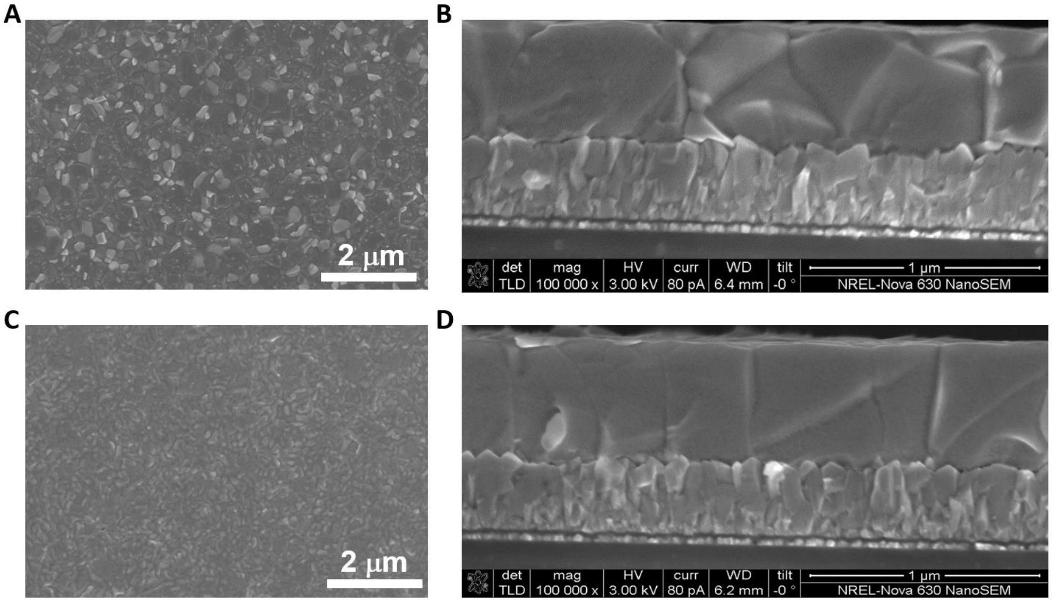

Fig. S14. Top view SEM images of (**A**) the control and (**C**) DMePDAI$_2$-modified perovskite thin films (scale bar: 2 μm). Cross-sectional view SEM images of (**B**) the control and (**D**) DMePDAI$_2$-modified perovskite thin films on FTO glass.

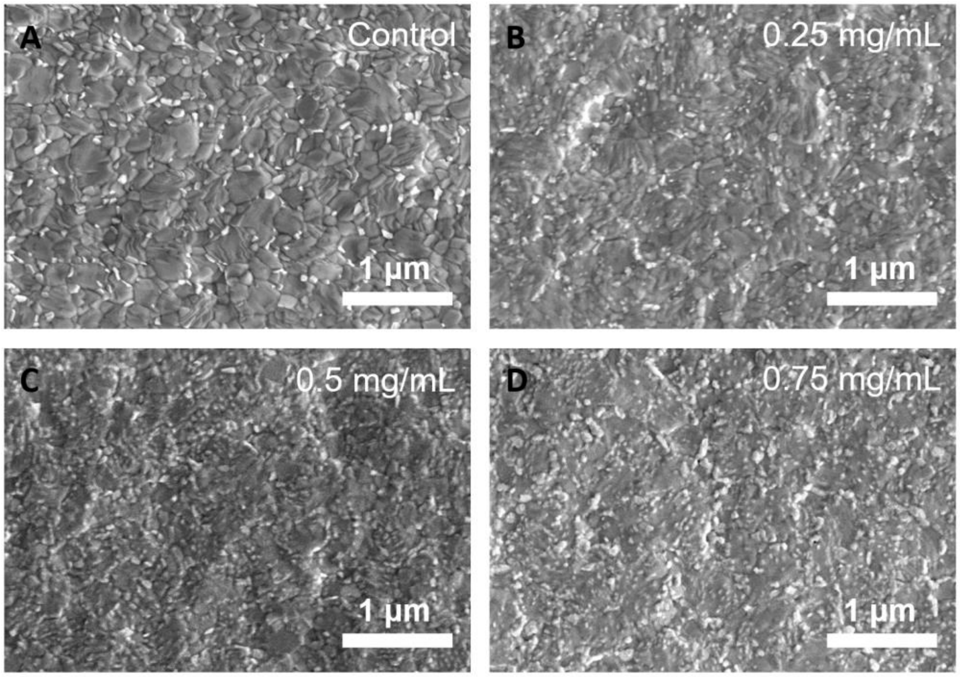

Fig. S15. (**A–D**) Top-view SEM images of perovskite thin films without (control; A) and with $DMePDAI_2$ surface treatment (B–D). The concentration of $DMePDAI_2$/IPA solution is varied from 0.25 mg/mL to 0.75 mg/mL as indicated. It shows that with increasing $DMePDAI_2$ solution concentration, the perovskite film surface smoothness is enhanced, and the perovskite grain boundaries gradually disappear.

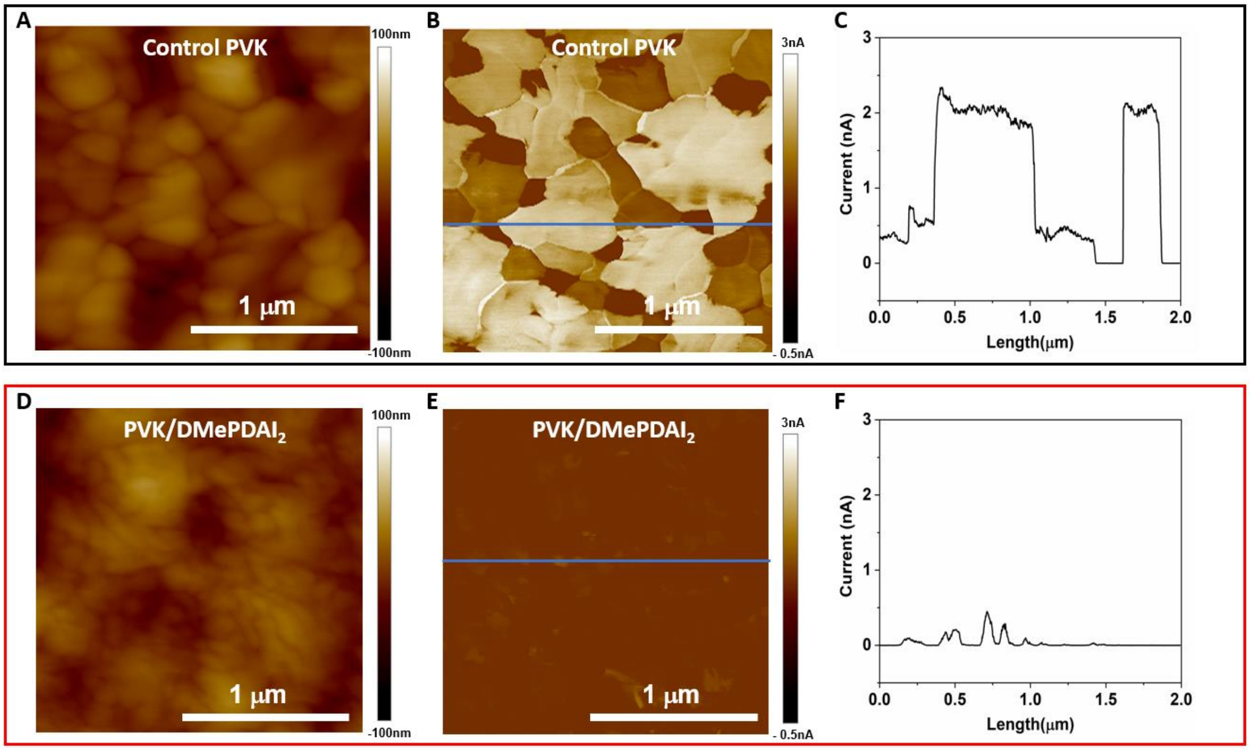

Fig. S16. AFM topography of (**A**) the control and (**D**) DMePDAI$_2$-modified perovskite thin films (scale bar: 1 μm). C-AFM images of (**B**) the control and (**E**) DMePDAI$_2$-modified perovskite thin films on TiO$_2$/FTO glass (scale bar: 1 μm). The corresponding line profiles of C-AFM based on (**C**) the control and (**F**) DMePDAI$_2$-modified perovskite thin films.

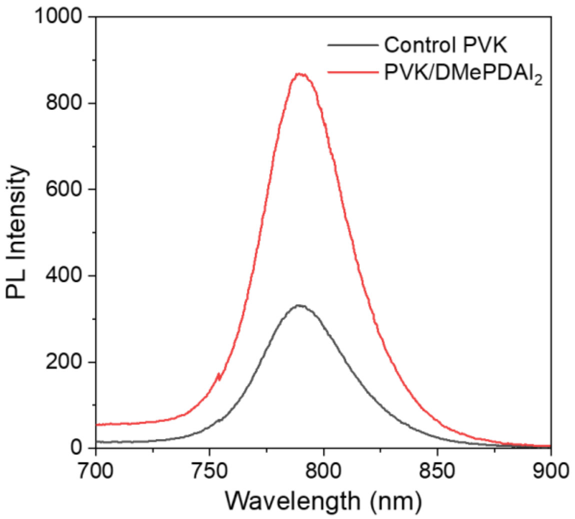

Fig. S17. Comparison of the PL measurements of the control and DMePDAI$_2$-modified perovskite thin films.

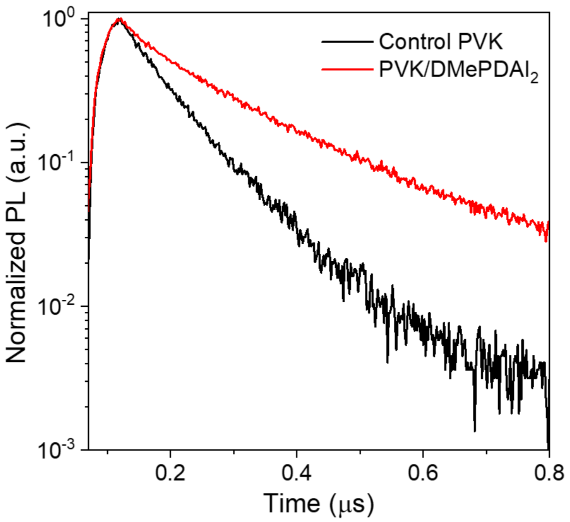

Fig. S18. Comparison of the TRPL measurements of the control and DMePDAI$_2$-modified perovskite thin films.

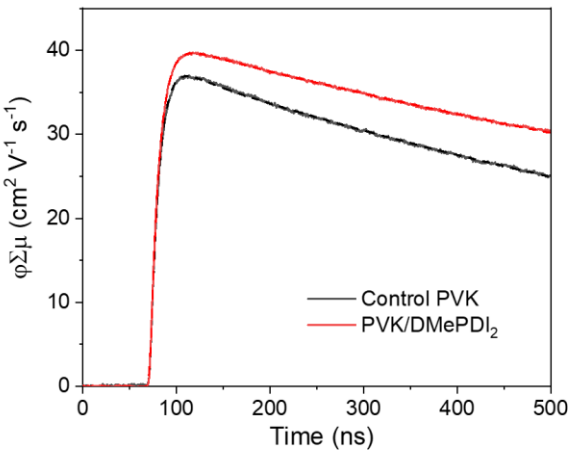

Fig. S19. Comparison of time-resolved microwave conductivity (TRMC) measurement of the control and DMePDAI$_2$-modified perovskite thin films. The control perovskite has a biexponential fitted average lifetime of 0.91 microseconds, while the DMePDAI$_2$-treated films lifetime had improved lifetimes of 1.32 microseconds, respectively. The fit-extracted t=0 yield-mobility product (φΣμ) value was found to be 36.9 cm^2/Vs, and 39.7 cm^2/Vs for the control, and DMePDAI$_2$ treated films, respectively. Since the yield is normally close to unity in high-performance PSCs, the yield-mobility product can be viewed as a measurement of the charge mobility.

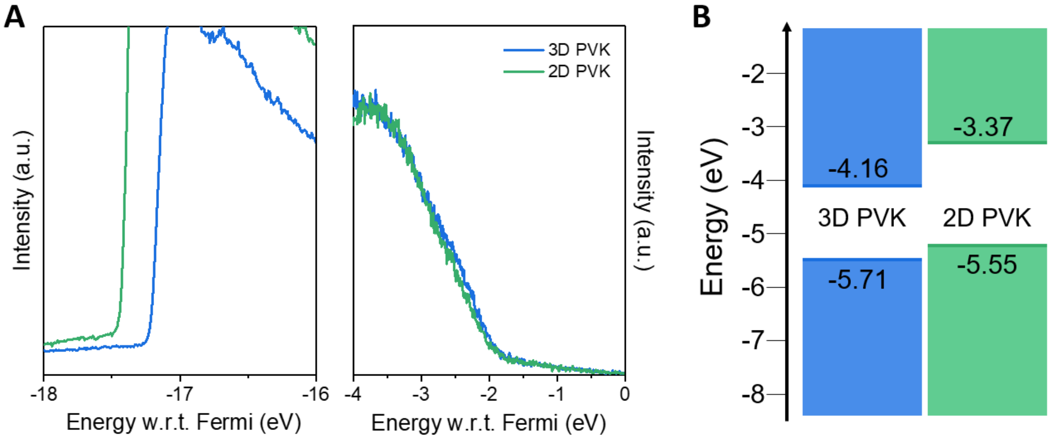

Fig. S20. (**A**) Ultraviolet photoelectron spectra (UPS) of the 3D perovskite film (3D PVK) and the 2D perovskite (2D PVK) coated on top of the 3D perovskite film. The baseline 3D perovskite composition is $FA_{0.85}MA_{0.1}Cs_{0.05}PbI_{2.9}Br_{0.1}$. (**B**) Schematic energy levels of the 3D and 2D perovskites in this study.

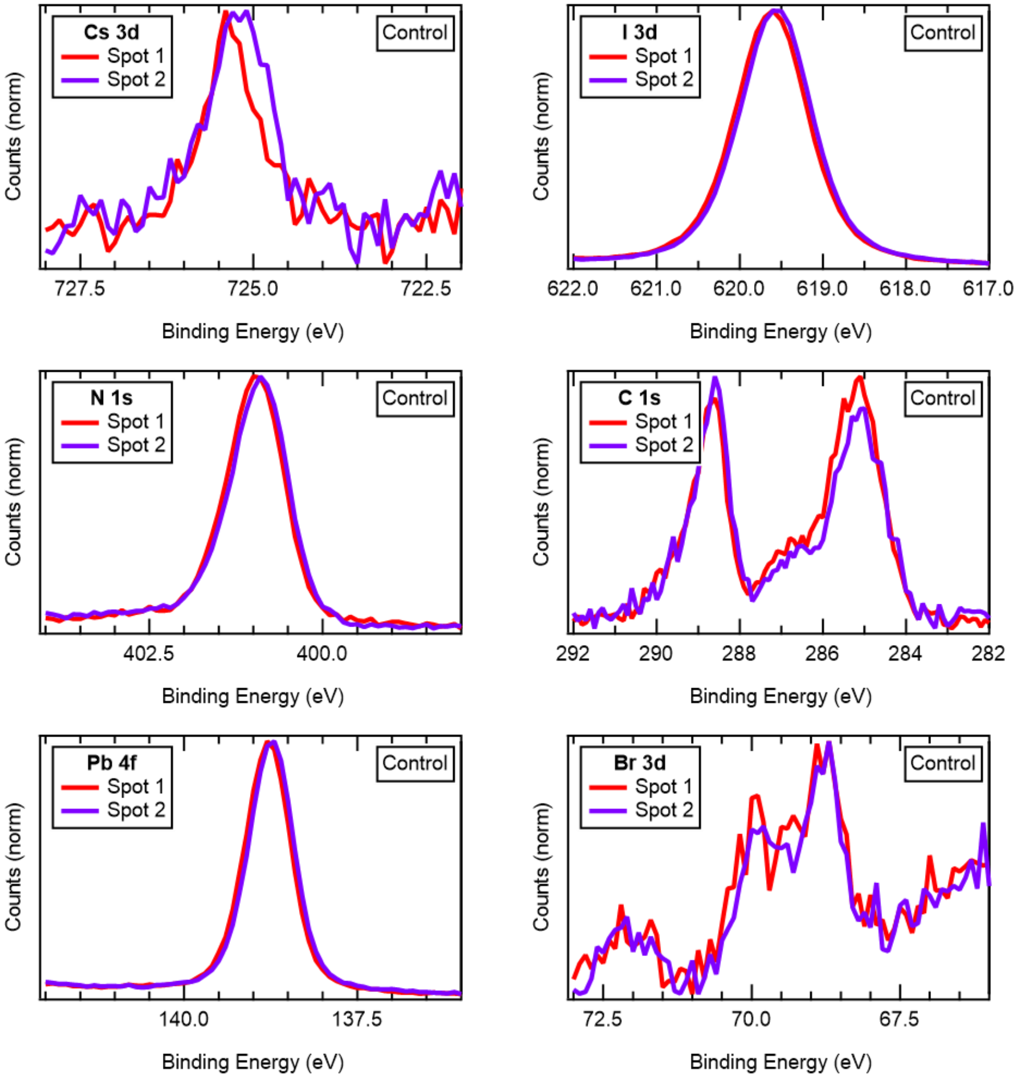

Fig. S21. The XPS spectra taken on two different spots based on the control perovskite thin film.

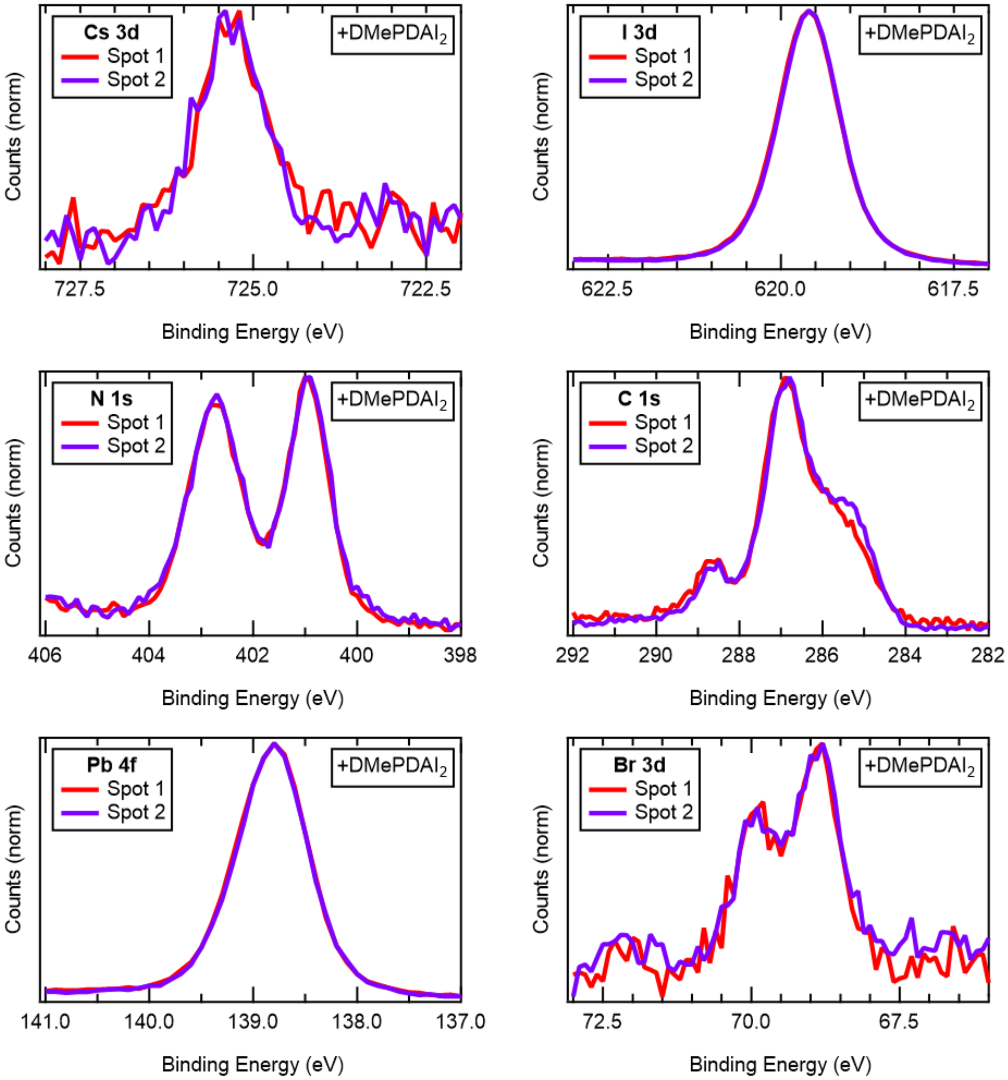

Fig. S22. The XPS spectra taken on two different spots on the DMePDAI$_2$-modified perovskite thin film.

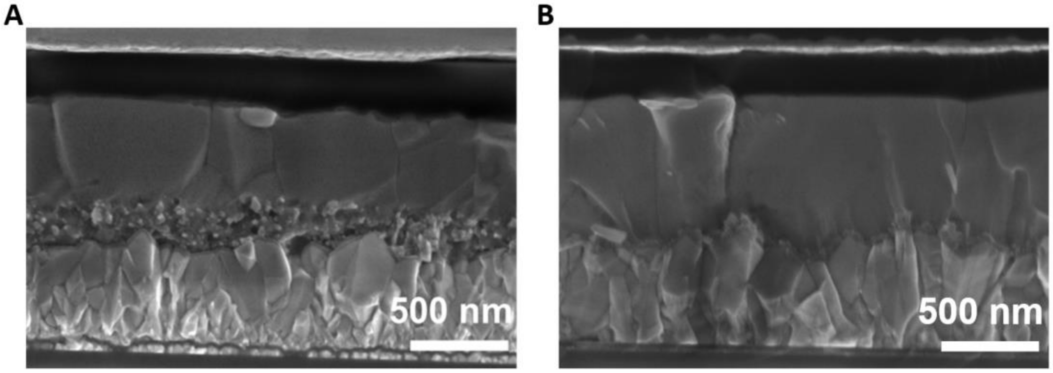

Fig. S23. Cross-sectional view SEM image of DMePDAI$_2$-modified perovskite-based device stack. (**A**) The cell architecture (from top to bottom) is Au/spiro-OMeTAD/FA$_{0.85}$MA$_{0.1}$Cs$_{0.05}$PbI$_{2.9}$Br$_{0.1}$ /mesoporous-TiO$_2$/compact-TiO$_2$/FTO/glass. (**B**) The cell architecture is Au/spiro-OMeTAD/ FA$_{0.97}$MA$_{0.03}$PbI$_{2.91}$Br$_{0.09}$/SnO$_2$/FTO/glass.

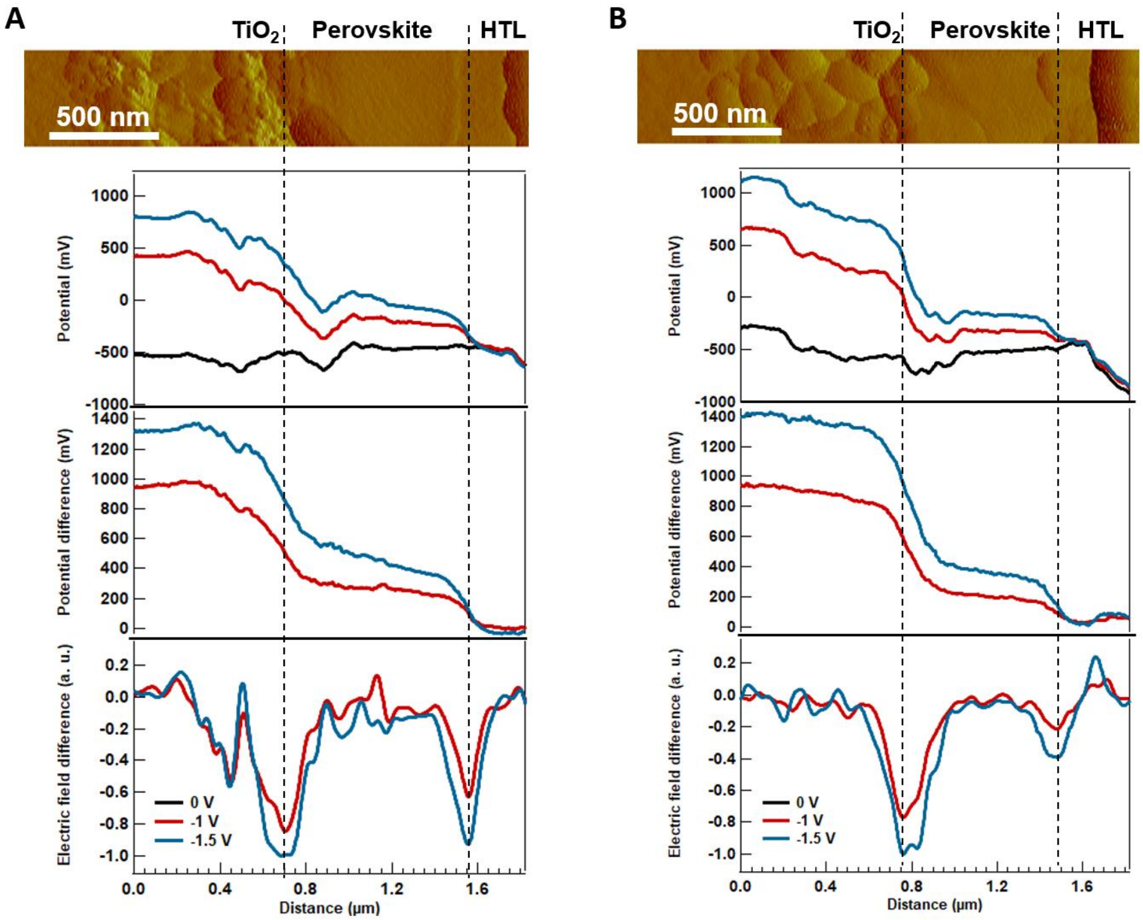

Fig. S24. KPFM electrical potential and field profiling on the cross-sectional surface for devices based on (**A**) the control and (**B**) DMePDAI$_2$-modified perovskite thin films. Top: potential profile under 0 V, -1 V, and -1.5 V bias voltages. Middle: potential difference between the various applied bias voltages and 0 V. Bottom: change in electric field calculated by taking the first derivatives of the potential difference. The hole transport layer (HTL) is spiro-OMeTAD. The local voltage drop across the device is determined by the competition of equivalent resistance of different layers and interfaces, which can be related to the interface quality. Because the electron transport layer (ETL)/perovskite interface should be identical for these devices, we normalized the ETL/perovskite peak to compare the “back-contact” quality at the perovskite/HTL interfaces between the surface-modified devices. It is evident that the DMePDAI$_2$-modified device showed a significantly smaller perovskite/HTL electric field difference peak than that of the control perovskite devices. If consider the main junction at ETL/perovskite interface, the smaller perovskite/HTL peak indicates that the DMePDAI$_2$-modified device has a less leaky interface (*44*), suggesting that a better back contact quality can decrease the energy loss associated with carrier transport over the interface, enabling higher FF and V_{oc} in devices.

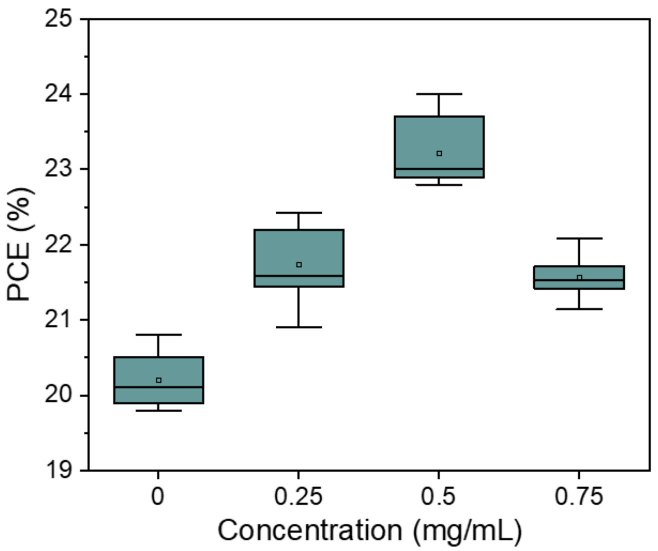

Fig. S25. Statistical distribution of PCE of perovskite solar cells based on $DMePDAI_2$-modified perovskite thin films with different concentrations. The control devices are those noted with zero concentration of surface treatment.

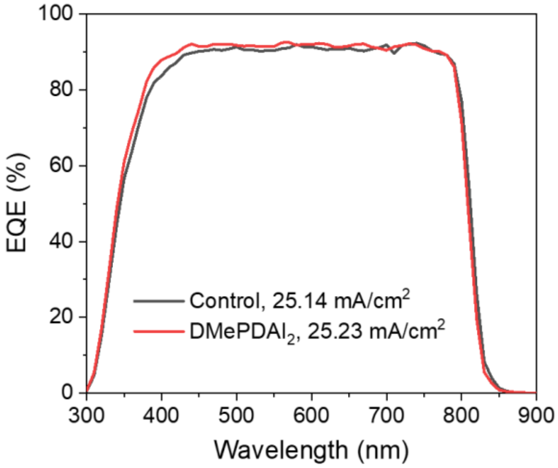

Fig. S26. EQE spectra with integrated current densities for the corresponding devices based on $FA_{0.97}MA_{0.03}PbI_{2.91}Br_{0.09}$-based devices without (Control) and with $DMePDAI_2$ surface modification ($DMePDAI_2$).

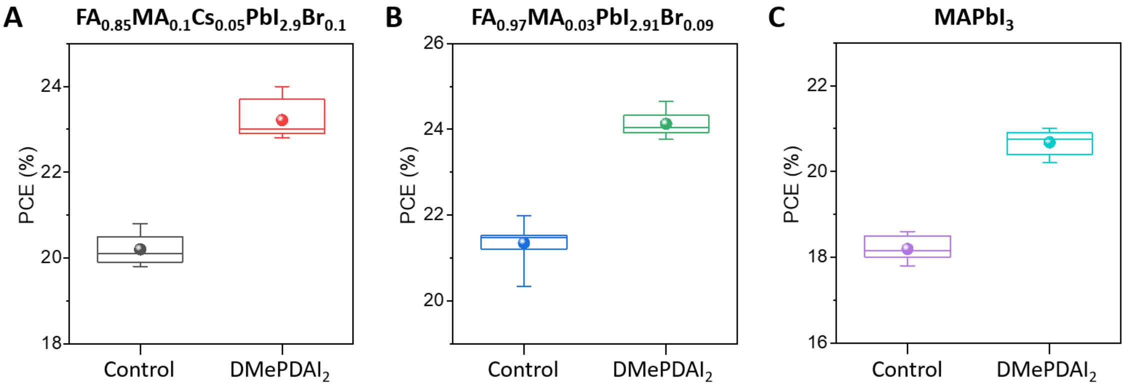

Fig. S27. Statistical comparison of PCEs for solar cells without (Control) and with $DMePDAI_2$ surface modification ($DMePDAI_2$) using three perovskite compositions: (**A**) $FA_{0.85}MA_{0.1}Cs_{0.05}PbI_{2.9}Br_{0.1}$, (**B**) $FA_{0.97}MA_{0.03}PbI_{2.91}Br_{0.09}$, and (**C**) $MAPbI_3$.

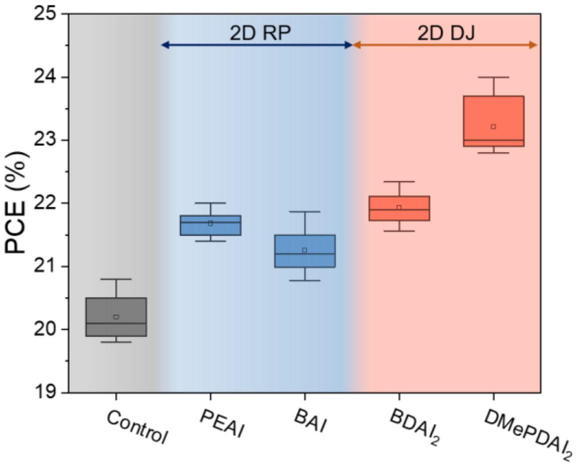

Fig. S28. Statistical PCE comparision of PSCs based on the control and different surface treated perovskite thin films. Organo-halide salts including phenethylammonium iodide (PEAI), butylammonium iodide (BAI), and 1,4-butane diammonium iodide ($BDAI_2$) for 2D materials have similar carbon chain length. In this series, PEAI and BAI are known to form RP 2D structures, whereas $BDAI_2$ is a symmetric molecule that can form DJ 2D structure of $BDAPbI_4$.

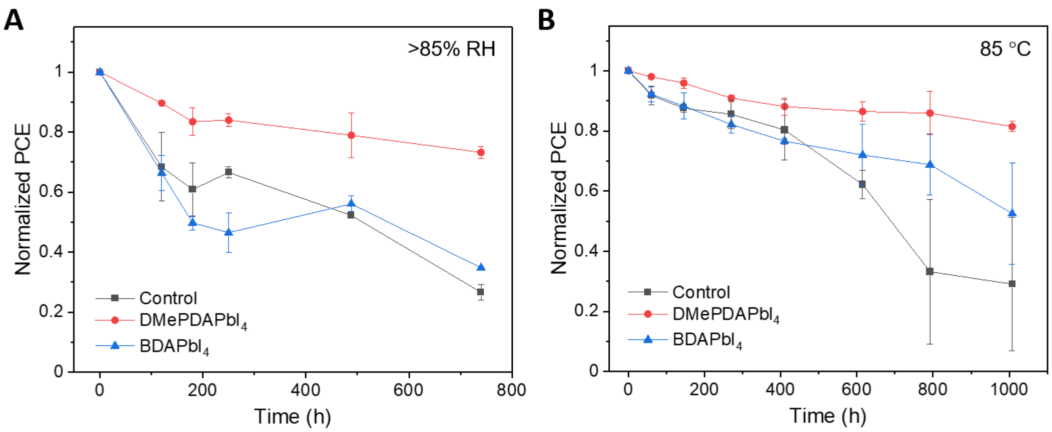

Fig. S29. Comparison of the moisture and thermal stability of PSCs without and with surface treatments. The baseline perovskite composition is $FA_{0.85}MA_{0.1}Cs_{0.05}PbI_{2.9}Br_{0.1}$. The PSC without surface treatment is the control. The PSC with $DMePDAI_2$ treatement is denoted by $DMePDAPbI_4$, and the PSC with $BDAI_2$ surface treatment is denoted by $BDAPbI_4$. Here, PTAA with 5 wt%TPFB was used to avoid the effect of hygroscopic additives and thermal degradation in spiro-OMeTAD. (**A**) Comparison of the moisture stability test of unencapsulated PSCs without and with surface treatment (as indicated) in 85% RH at room temperature for 740 h. The average PCE of unencapsulated control, $BDAI_2$-treated, and $DMePDAI_2$-treated PSCs maintained about 27%, 35%, 73% of their respective initial PCEs after 740 h ageing under >85% RH. The increased stability of $DMePDAI_2$-treated PSCs relative to $BDAI_2$-treated ones is consistent with the increased hydrophobicity (Figure S30). (**B**) Comparison of the thermal stability test of unencapsulated PSCs without and with surface treatment (as indicated) heated at 85°C for 1008 h, in dark, 5% RH. The average PCE of unencapsulated control, $BDAI_2$-treated, and $DMePDAI_2$-treated PSCs maintained about 29%, 53% and 81% of their respective initial PCEs after 1008-h ageing at 85°C.

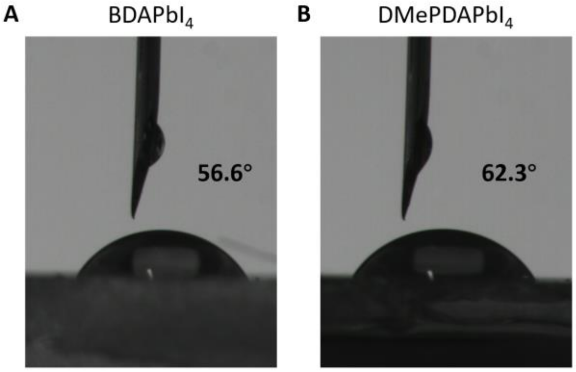

Fig. S30. Comparison of contact angle measurement of (**A**) $BDAPbI_4$ and (**B**) $DMePDAPbI_4$ perovskite thin films.

Table S1. Crystal Data and Structure Refinement for $[PDAPbI_4]_{15}$•$[PDAI_2]$

	Compound Name $[PDAPbI_4]_{15}$•$[PDAI_2]$
Empirical formula	$C_{48}H_{192}I_{62}N_{32}Pb_{15}$
Formula weight	12193.97
Temperature	90.0(2) K
Wavelength	0.71073 Å
Crystal system	Monoclinic
Space group	Cc
Unit cell dimensions	a = 45.3082(10) Å b = 15.9410(3) Å, β = 107.745(1)° c = 31.3446(7) Å
Volume	21561.8(8) $Å^3$
Z	4
Density (calculated)	3.756 g/cm^3
Absorption coefficient	20.575 mm^{-1}
F(000)	20880
Crystal size	0.060 × 0.050 × 0.030 mm^3
θ range for data collection	2.336 to 27.493°
Index ranges	-58<=h<=58, -20<=k<=20, -40<=l<=40
Reflections collected	446291
Independent reflections	49316 [R_{int} = 0.0757]
Completeness to θ = 25.242°	99.9%
Refinement method	Full-matrix least-squares on F^2
Data / restraints / parameters	49316 / 1116 / 1535
Goodness-of-fit	1.048
Final R indices [I > 2σ(I)]	R_{obs} = 0.0305, wR_{obs} = 0.0439
R indices [all data]	R_{all} = 0.0392, wR_{all} = 0.0463
Largest diff. peak and hole	1.770 and -1.961 e·$Å^{-3}$

$R = \Sigma||F_o|-|F_c|| / \Sigma|F_o|$, $wR = \{\Sigma[w(|F_o|^2 - |F_c|^2)^2] / \Sigma[w(|F_o|^4)]\}^{1/2}$ and $w=1/[\sigma^2(Fo^2)+0.8092P]$ where $P=(Fo^2+2Fc^2)/3$

Table S2. Crystal Data and Structure Refinement for $BDAPbI_4$

	Compound Name
	$BDAPbI_4$
Empirical formula	$C_4H_{14}I_4N_2Pb$
Formula weight	804.96
Temperature	90.0 (2) K
Wavelength	0.71073 Å
Crystal system	triclinic
Space group	*P-1*
Unit cell dimensions	a = 8.4730(3)Å, α = 76.703° b = 8.7791(3)Å, β = 70.236 (1)° c = 11.0538(4)Å, γ = 89.241°
Volume	751.19(5) $Å^3$
Z	2
Density (calculated)	3.559 g/cm^3
Absorption coefficient	19.410 mm^{-1}
F(000)	692
Crystal size	0.150 × 0.110 × 0.100 mm^3
θ range for data collection	2.39 to 27.51°
Index ranges	$-11 \leq h \leq 11, -11 \leq k \leq 11, -14 \leq l \leq 14$
Reflections collected	3412
Independent reflections	3235
Completeness to θ = 25.242°	99.5%
Refinement method	Full-matrix least-squares on F^2
Data / restraints / parameters	3412 / 0 / 106
Goodness-of-fit	1.226
Final R indices [I > 2σ(I)]	$R_{obs} = 0.0192$, $wR_{obs} = 0.0399$
R indices [all data]	$R_{all} = 0.0220$, $wR_{all} = 0.0405$
Extinction coefficient	0.00141
Largest diff. peak and hole	1.203 and -1.059 $e{\cdot}Å^{-3}$

$R = \Sigma||F_o|-|F_c|| / \Sigma|F_o|$, $wR = \{\Sigma[w(|F_o|^2 - |F_c|^2)^2] / \Sigma[w(|F_o|^4)]\}^{1/2}$ and $w=1/[\sigma^2(Fo^2)+1.254P]$ where $P=(Fo^2+2Fc^2)/3$

Table S3. Crystal Data and Structure Refinement for DMePDAPbI_4-1

	Compound Name
	DMePDAPbI_4-1
Empirical formula	$C_5H_{16}I_4N_2Pb$
Formula weight	818.99
Temperature	90.0 (2) K
Wavelength	0.71073 Å
Crystal system	Monoclinic
Space group	*P*2_1/c
Unit cell dimensions	a = 11.0940(3) Å b = 12.3733(2) Å, β = 112.652 (1)° c = 12.7504(3) Å
Volume	1615.23(6) Å^3
Z	4
Density (calculated)	3.368 g/cm^3
Absorption coefficient	18.060 mm^{-1}
F(000)	1416
Crystal size	0.110 x 0.100 x 0.060 mm^3
θ range for data collection	2.582 to 27.515°
Index ranges	-14<=h<=13, 0<=k<=16, 0<=l<=16
Reflections collected	3711
Independent reflections	3711
Completeness to θ = 25.242°	99.3%
Refinement method	Full-matrix least-squares on F^2
Data / restraints / parameters	3711 / 0 / 114
Goodness-of-fit	1.123
Final R indices [I > 2σ(I)]	R_{obs} = 0.0157, wR_{obs} = 0.0385
R indices [all data]	R_{all} = 0.0165, wR_{all} = 0.0387
Extinction coefficient	0.00194(8)
Largest diff. peak and hole	0.898 and -0.810 e·Å^{-3}

$R = \Sigma||F_o|-|F_c|| / \Sigma|F_o|$, $wR = \{\Sigma[w(|F_o|^2 - |F_c|^2)^2] / \Sigma[w(|F_o|^4)]\}^{1/2}$ and $w=1/[\sigma^2(Fo^2)+(0.0150P)^2+1.7692P]$ where $P=(Fo^2+2Fc^2)/3$

Table S4. Performance parameters of perovskite solar cells based on perovskite thin films of different bulky cations (n=1) under different scan directions with a bias step of 10 mV. (V_{oc}: open-circuit voltage; J_{sc}: short-circuit current density; FF: fill factor; PCE: power conversion efficiency).

Device	**Scan**	**J_{sc} (mA/cm^2)**	**V_{oc} (V)**	**FF**	**PCE (%)**
$DMePDAPbI_4$	Forward	6.98	1.01	0.69	4.90
	Reverse	7.01	1.01	0.66	4.33
$BDAPbI_4$	Forward	4.85	0.91	0.61	2.69
	Reverse	4.81	0.92	0.47	2.08
PEA_2PbI_4	Forward	2.61	0.91	0.59	1.40
	Reverse	2.60	0.90	0.46	1.07
BA_2PbI_4	Forward	2.56	0.88	0.57	1.28
	Reverse	2.50	0.88	0.41	0.90

Table S5. Lifetimes of the control, and $DMePDAI_2$-modified perovskite thin films extracted by fitting the PL decay curve with a bi-exponential decay function.

Samples	fast component τ_1 (ns)	slow component τ_2 (ns)
Control	50	101
$DMePDAI_2$	61	181

Table S6. The constrained fitting procedure (from low binding energy [BE] to high) used by deconvoluted C1s peak.

Peak #	BE location	FWHM
C-C/C-H	-1.7 to -1.4	1.3 – 1.4
C-NH_3	x	1.15 – 1.25
HC(NH_2)	+1.75 to +1.85	0.9 – 1.1
C-O/C=O	+2.75 to +2.85	1.25 – 1.35

Table S7. The constrained fitting procedure (from low binding energy [BE] to high) used by deconvoluted N1s peak.

Peak #	BE location	FWHM
CH_2-NH^+-$(CH_3)_2$	-2.35 to -2.25	1.8 – 2.0
C-NH_2	-1.2 to -1.1	0.8 – 1.0
C=NH_2^+	x	0.95 – 1.0
C-NH_3	+1.6 to +1.8	1.15 – 1.25

References and Notes

1. R.-C. E. C. Best, National Renewable Energy Laboratory, https://www.nrel.gov/pv/cell-efficiency.html (Augest,2020)

2. D. Bi, C. Yi, J. Luo, J.-D. Décoppet, F. Zhang, S. M. Zakeeruddin, X. Li, A. Hagfeldt, M. Grätzel, Polymer-templated nucleation and crystal growth of perovskite films for solar cells with efficiency greater than 21%. *Nat. Energy* **1**, 16142 (2016). doi:10.1038/nenergy.2016.142

3. X. Zheng, B. Chen, J. Dai, Y. Fang, Y. Bai, Y. Lin, H. Wei, X. C. Zeng, J. Huang, Defect passivation in hybrid perovskite solar cells using quaternary ammonium halide anions and cations. *Nat. Energy* **2**, 17102 (2017). doi:10.1038/nenergy.2017.102

4. F. Zhang, W. Shi, J. Luo, N. Pellet, C. Yi, X. Li, X. Zhao, T. J. S. Dennis, X. Li, S. Wang, Y. Xiao, S. M. Zakeeruddin, D. Bi, M. Grätzel, Isomer-pure bis-PCBM-assisted crystal engineering of perovskite solar cells showing excellent efficiency and stability. *Adv. Mater.* **29**, 1606806 (2017). doi:10.1002/adma.201606806 Medline

5. X. Li, M. I. Dar, C. Yi, J. Luo, M. Tschumi, S. M. Zakeeruddin, M. K. Nazeeruddin, H. Han, M. Grätzel, Improved performance and stability of perovskite solar cells by crystal crosslinking with alkylphosphonic acid ω-ammonium chlorides. *Nat. Chem.* **7**, 703–711 (2015). doi:10.1038/nchem.2324 Medline

6. F. Zhang, H. Lu, J. Tong, J. J. Berry, M. C. Beard, K. Zhu, Advances in two-dimensional organic–inorganic hybrid perovskites. *Energy Environ. Sci.* **13**, 1154–1186 (2020). doi:10.1039/C9EE03757H

7. E. H. Jung, N. J. Jeon, E. Y. Park, C. S. Moon, T. J. Shin, T.-Y. Yang, J. H. Noh, J. Seo, Efficient, stable and scalable perovskite solar cells using poly(3-hexylthiophene). *Nature* **567**, 511–515 (2019). doi:10.1038/s41586-019-1036-3 Medline

8. H. Min, M. Kim, S.-U. Lee, H. Kim, G. Kim, K. Choi, J. H. Lee, S. I. Seok, Efficient, stable solar cells by using inherent bandgap of α-phase formamidinium lead iodide. *Science* **366**, 749–753 (2019). doi:10.1126/science.aay7044 Medline

9. L. Liang, H. Luo, J. Hu, H. Li, P. Gao, Efficient perovskite solar cells by reducing interface-mediated recombination: A bulky amine approach. *Adv. Energy Mater.* **10**, 2000197 (2020). doi:10.1002/aenm.202000197

10. Y.-W. Jang, S. Lee, K. M. Yeom, K. Jeong, K. Choi, M. Choi, J. H. Noh, Intact 2D/3D halide junction perovskite solar cells via solid-phase in-plane growth. *Nat. Energy* **6**, 63–71 (2021). doi:10.1038/s41560-020-00749-7

11. J. Xue, R. Wang, X. Chen, C. Yao, X. Jin, K.-L. Wang, W. Huang, T. Huang, Y. Zhao, Y. Zhai, D. Meng, S. Tan, R. Liu, Z.-K. Wang, C. Zhu, K. Zhu, M. C. Beard, Y. Yan, Y. Yang, Reconfiguring the band-edge states of photovoltaic perovskites by conjugated organic cations. *Science* **371**, 636–640 (2021). doi:10.1126/science.abd4860 Medline

12. D. Thrithamarassery Gangadharan, D. Ma, Searching for stability at lower dimensions: Current trends and future prospects of layered perovskite solar cells. *Energy Environ. Sci.* **12**, 2860–2889 (2019). doi:10.1039/C9EE01591D

13. E. Shi, B. Yuan, S. B. Shiring, Y. Gao, Y. Akriti, Y. Guo, C. Su, M. Lai, P. Yang, J. Kong, B. M. Savoie, Y. Yu, L. Dou, Two-dimensional halide perovskite lateral epitaxial heterostructures. *Nature* **580**, 614–620 (2020). doi:10.1038/s41586-020-2219-7 Medline

14. Y. Gao, E. Shi, S. Deng, S. B. Shiring, J. M. Snaider, C. Liang, B. Yuan, R. Song, S. M. Janke, A. Liebman-Peláez, P. Yoo, M. Zeller, B. W. Boudouris, P. Liao, C. Zhu, V. Blum, Y. Yu, B. M. Savoie, L. Huang, L. Dou, Molecular engineering of organic-inorganic hybrid perovskites quantum wells. *Nat. Chem.* **11**, 1151–1157 (2019). doi:10.1038/s41557-019-0354-2 Medline

15. S. Ahmad, P. Fu, S. Yu, Q. Yang, X. Liu, X. Wang, X. Wang, X. Guo, C. Li, Dion-Jacobson phase 2D layered perovskites for solar cells with ultrahigh stability. *Joule* **3**, 794–806 (2019). doi:10.1016/j.joule.2018.11.026

16. L. Mao, W. Ke, L. Pedesseau, Y. Wu, C. Katan, J. Even, M. R. Wasielewski, C. C. Stoumpos, M. G. Kanatzidis, Hybrid Dion–Jacobson 2D lead iodide perovskites. *J. Am. Chem. Soc.* **140**, 3775–3783 (2018). doi:10.1021/jacs.8b00542 Medline

17. Y. Lv, H. Ma, Y. Yin, Q. Dong, W. Zhao, S. Jin, Y. Shi, $[NH_3(CH_2)_6NH_3]PbI_4$ as Dion–Jacobson phase bifunctional capping layer for 2D/3D perovskite solar cells with high efficiency and excellent UV stability. *J. Mater. Chem. A Mater. Energy Sustain.* **8**, 10283–10290 (2020). doi:10.1039/D0TA02437F

18. X. Jiang, J. Zhang, S. Ahmad, D. Tu, X. Liu, G. Jia, X. Guo, C. Li, Dion-Jacobson 2D-3D perovskite solar cells with improved efficiency and stability. *Nano Energy* **75**, 104892 (2020). doi:10.1016/j.nanoen.2020.104892

19. X. Li, J. M. Hoffman, M. G. Kanatzidis, The 2D halide perovskite rulebook: How the spacer influences everything from the structure to optoelectronic device efficiency. *Chem. Rev.* **121**, 2230–2291 (2021). doi:10.1021/acs.chemrev.0c01006 Medline

20. G. L. F. Miessler, P. J.; Tarr, D. A., *Inorganic Chemistry*. (Prentice Hall: Upper Saddle Rive, NJ, ed. 5th Edition, 2014).

21. C. Ma, D. Shen, T.-W. Ng, M.-F. Lo, C.-S. Lee, C.-S. Lee, 2D perovskites with short interlayer distance for high-performance solar cell application. *Adv. Mater.* **30**, 1800710 (2018). doi:10.1002/adma.201800710

22. T. Yu, L. Zhang, J. Shen, Y. Fu, Y. Fu, Hydrogen bonds and steric effects induced structural modulation of three layered iodoplumbate hybrids from nonperovskite to perovskite structure. *Dalton Trans.* **43**, 13115–13121 (2014). doi:10.1039/C4DT01181C Medline

23. F. Zhang, H. Lu, B. W. Larson, C. Xiao, S. P. Dunfield, O. G. Reid, X. Chen, M. Yang, J. J. Berry, M. C. Beard, K. Zhu, Surface lattice engineering through three-dimensional lead iodide perovskitoid for high-performance perovskite solar cells. *Chem* **7**, 774–785 (2021). doi:10.1016/j.chempr.2020.12.023

24. S. Silver, S. Xun, H. Li, J.-L. Brédas, A. Kahn, Structural and electronic impact of an asymmetric organic ligand in diammonium lead iodide perovskites. *Adv. Energy Mater.* **10**, 1903900 (2020). doi:10.1002/aenm.201903900

25. W. Zhao, Q. Dong, J. Zhang, S. Wang, M. Chen, C. Zhao, M. Hu, S. Jin, N. P. Padture, Y. Shi, Asymmetric alkyl diamine based Dion–Jacobson low-dimensional perovskite solar

cells with efficiency exceeding 15%. *J. Mater. Chem. A Mater. Energy Sustain.* **8**, 9919–9926 (2020). doi:10.1039/D0TA02706E

26. A. V. Krukau, O. A. Vydrov, A. F. Izmaylov, G. E. Scuseria, Influence of the exchange screening parameter on the performance of screened hybrid functionals. *J. Chem. Phys.* **125**, 224106 (2006). doi:10.1063/1.2404663 Medline

27. S. Grimme, J. Antony, S. Ehrlich, H. Krieg, A consistent and accurate ab initio parametrization of density functional dispersion correction (DFT-D) for the 94 elements H-Pu. *J. Chem. Phys.* **132**, 154104 (2010). doi:10.1063/1.3382344 Medline

28. F. Zhang, D. H. Kim, H. Lu, J.-S. Park, B. W. Larson, J. Hu, L. Gao, C. Xiao, O. G. Reid, X. Chen, Q. Zhao, P. F. Ndione, J. J. Berry, W. You, A. Walsh, M. C. Beard, K. Zhu, Enhanced Charge Transport in 2D Perovskites via Fluorination of Organic Cation. *J. Am. Chem. Soc.* **141**, 5972–5979 (2019). doi:10.1021/jacs.9b00972 Medline

29. D. L. McGott, C. P. Muzzillo, C. L. Perkins, J. J. Berry, K. Zhu, J. N. Duenow, E. Colegrove, C. A. Wolden, M. O. Reese, 3D/2D passivation as a secret to success for polycrystalline thin-film solar cells. *Joule* **5**, 1057–1073 (2021). doi:10.1016/j.joule.2021.03.015

30. H. Zhu, Y. Ren, L. Pan, O. Ouellette, F. T. Eickemeyer, Y. Wu, X. Li, S. Wang, H. Liu, X. Dong, S. M. Zakeeruddin, Y. Liu, A. Hagfeldt, M. Grätzel, Synergistic Effect of Fluorinated Passivator and Hole Transport Dopant Enables Stable Perovskite Solar Cells with an Efficiency Near 24. *J. Am. Chem. Soc.* **143**, 3231–3237 (2021). doi:10.1021/jacs.0c12802 Medline

31. S. P. Dunfield, L. Bliss, F. Zhang, J. M. Luther, K. Zhu, M. F. A. M. Hest, M. O. Reese, J. J. Berry, From defects to degradation: A mechanistic understanding of degradation in perovskite solar cell devices and modules. *Adv. Energy Mater.* **10**, 1904054 (2020). doi:10.1002/aenm.201904054

32. Y. Hou, E. Aydin, M. De Bastiani, C. Xiao, F. H. Isikgor, D.-J. Xue, B. Chen, H. Chen, B. Bahrami, A. H. Chowdhury, A. Johnston, S.-W. Baek, Z. Huang, M. Wei, Y. Dong, J. Troughton, R. Jalmood, A. J. Mirabelli, T. G. Allen, E. Van Kerschaver, M. I. Saidaminov, D. Baran, Q. Qiao, K. Zhu, S. De Wolf, E. H. Sargent, Efficient tandem solar cells with solution-processed perovskite on textured crystalline silicon. *Science* **367**, 1135–1140 (2020). doi:10.1126/science.aaz3691 Medline

33. M. V. Khenkin, E. A. Katz, A. Abate, G. Bardizza, J. J. Berry, C. Brabec, F. Brunetti, V. Bulović, Q. Burlingame, A. Di Carlo, R. Cheacharoen, Y.-B. Cheng, A. Colsmann, S. Cros, K. Domanski, M. Dusza, C. J. Fell, S. R. Forrest, Y. Galagan, D. Di Girolamo, M. Grätzel, A. Hagfeldt, E. von Hauff, H. Hoppe, J. Kettle, H. Köbler, M. S. Leite, S. Liu, Y.-L. Loo, J. M. Luther, C.-Q. Ma, M. Madsen, M. Manceau, M. Matheron, M. McGehee, R. Meitzner, M. K. Nazeeruddin, A. F. Nogueira, Ç. Odabaşı, A. Osherov, N.-G. Park, M. O. Reese, F. De Rossi, M. Saliba, U. S. Schubert, H. J. Snaith, S. D. Stranks, W. Tress, P. A. Troshin, V. Turkovic, S. Veenstra, I. Visoly-Fisher, A. Walsh, T. Watson, H. Xie, R. Yıldırım, S. M. Zakeeruddin, K. Zhu, M. Lira-Cantu, Consensus statement for stability assessment and reporting for perovskite photovoltaics based on ISOS procedures. *Nat. Energy* **5**, 35–49 (2020). doi:10.1038/s41560-019-0529-5

34. E. H. Anaraki, A. Kermanpur, L. Steier, K. Domanski, T. Matsui, W. Tress, M. Saliba, A. Abate, M. Grätzel, A. Hagfeldt, J.-P. Correa-Baena, Highly efficient and stable planar

perovskite solar cells by solution-processed tin oxide. *Energy Environ. Sci.* **9**, 3128–3134 (2016). doi:10.1039/C6EE02390H

35. G. Ashiotis, A. Deschildre, Z. Nawaz, J. P. Wright, D. Karkoulis, F. E. Picca, J. Kieffer, The fast azimuthal integration Python library: *pyFAI*. *J. Appl. Crystallogr.* **48**, 510–519 (2015). doi:10.1107/S1600576715004306 Medline
36. C. L. Perkins, F. S. Hasoon, Surfactant-assisted growth of CdS thin films for photovoltaic applications. *J. Vac. Sci. Technol. A* **24**, 497–504 (2006). doi:10.1116/1.2194929
37. J. Even, L. Pedesseau, J.-M. Jancu, C. Katan, Importance of Spin–Orbit Coupling in Hybrid Organic/Inorganic Perovskites for Photovoltaic Applications. *J. Phys. Chem. Lett.* **4**, 2999–3005 (2013). doi:10.1021/jz401532q
38. S. X. Tao, X. Cao, P. A. Bobbert, Accurate and efficient band gap predictions of metal halide perovskites using the DFT-1/2 method: GW accuracy with DFT expense. *Sci. Rep.* **7**, 14386 (2017). doi:10.1038/s41598-017-14435-4 Medline
39. M. Guidon, J. Hutter, J. VandeVondele, Auxiliary Density Matrix Methods for Hartree-Fock Exchange Calculations. *J. Chem. Theory Comput.* **6**, 2348–2364 (2010). doi:10.1021/ct1002225 Medline
40. J. Hutter, M. Iannuzzi, F. Schiffmann, J. VandeVondele, cp2k: atomistic simulations of condensed matter systems. *Wiley Interdiscip. Rev. Comput. Mol. Sci.* **4**, 15–25 (2014). doi:10.1002/wcms.1159
41. K. Wang, C. Wu, D. Yang, Y. Jiang, S. Priya, Quasi-Two-Dimensional Halide Perovskite Single Crystal Photodetector. *ACS Nano* **12**, 4919–4929 (2018). doi:10.1021/acsnano.8b01999 Medline
42. J. V. Passarelli, D. J. Fairfield, N. A. Sather, M. P. Hendricks, H. Sai, C. L. Stern, S. I. Stupp, Enhanced Out-of-Plane Conductivity and Photovoltaic Performance in n = 1 Layered Perovskites through Organic Cation Design. *J. Am. Chem. Soc.* **140**, 7313–7323 (2018). doi:10.1021/jacs.8b03659 Medline
43. A. B. Corradi, A. M. Ferrari, G. C. Pellacani, A. Saccani, F. Sandrolini, P. Sgarabotto, Structural and Electrical Characterization of Polymeric Haloplumbate(II) Systems. *Inorg. Chem.* **38**, 716–721 (1999). doi:10.1021/ic980893k
44. C. Xiao, C. Wang, W. Ke, B. P. Gorman, J. Ye, C.-S. Jiang, Y. Yan, M. M. Al-Jassim, Junction Quality of SnO_2-Based Perovskite Solar Cells Investigated by Nanometer-Scale Electrical Potential Profiling. *ACS Appl. Mater. Interfaces* **9**, 38373–38380 (2017). doi:10.1021/acsami.7b08582 Medline